A&A 537, A98 (2012)
DOI: 10.1051/0004-6361/201118201

Astronomy & Astrophysics

Water emission from the chemically rich outflow L1157

M. Vasta[1], C. Codella[1], A. Lorenzani[1], G. Santangelo[2], B. Nisini[2], T. Giannini[2], M. Tafalla[3], R. Liseau[4], E. F. van Dishoeck[5,6], and L. Kristensen[5]

[1] Osservatorio Astrofisico di Arcetri, Largo Enrico Fermi 5, 50125 Florence, Italy
e-mail: mvasta@arcetri.astro.it
[2] INAF, Osservatorio Astronomico di Roma, via di Frascati 33, 00040 Monteporzio Catone, Italy
[3] Observatorio Astronomico Nacional (IGN), Calle Alfonso XII 3, 28014 Madrid, Spain
[4] Department of Earth and Space Sciences, Chalmers University of Technology, Onsala Space Observatory, 439 92 Onsala, Sweden
[5] Leiden Observatory, Leiden University, PO Box 9513, 2300 RA Leiden, The Netherlands
[6] Max-Planck-Institut für Extraterrestrische Physik, Giessenbachstrasse 1, 85748 Garching, Germany

Received 4 October 2011 / Accepted 30 October 2011

ABSTRACT

Context. In the framework of the *Herschel*-WISH key program, several ortho-H_2O and para-H_2O emission lines, in the frequency range from 500 to 1700 GHz, were observed with the HIFI instrument in two bow-shock regions (B2 and R) of the L1157 cloud, which hosts what is considered to be the prototypical chemically-rich outflow.
Aims. Our primary aim is to analyse water emission lines as a diagnostic of the physical conditions in the blue (B2) and red-shifted (R) lobes to compare the excitation conditions.
Methods. For this purpose, we ran the non-LTE RADEX model for a plane-parallel geometry to constrain the physical parameters ($T_{\rm kin}$, $N_{\rm H_2O}$ and $n_{\rm H_2}$) of the water emission lines detected.
Results. A total of 5 ortho- and para-$H_2{}^{16}O$ plus one o$-H_2{}^{18}O$ transitions were observed in B2 and R with a wide range of excitation energies (27 K $\leq E_{\rm u} \leq$ 215 K). The H_2O spectra, observed in the two shocked regions, show that the H_2O profiles differ markedly in the two regions. In particular, at the bow-shock R, we observed broad (∼30 km s^{-1} with respect to the ambient velocity) red-shifted wings where lines at different excitation peak at different red-shifted velocities. The B2 spectra are associated with a narrower velocity range (∼6 km s^{-1}), peaking at the systemic velocity. The excitation analysis suggests, for B2, low values of column density $N_{\rm H_2O} \leq 5 \times 10^{13}$ cm^{-2}, a density range of $10^5 \leq n_{\rm H_2} \leq 10^7$ cm^{-3}, and warm temperatures (≥300 K). The presence of the broad red-shifted wings and multiple peaks in the spectra of the R region, prompted the modelling of two components. High velocities are associated with relatively low temperatures (∼100 K), $N_{\rm H_2O} \simeq 5 \times 10^{12}$–$5 \times 10^{13}$ cm^{-2} and densities $n_{\rm H_2} \simeq 10^6$–10^8 cm^{-3}. Lower velocities are associated with higher excitation conditions with $T_{\rm kin} \geq 300$ K, very dense gas ($n_{\rm H_2} \sim 10^8$ cm^{-3}) and low column density ($N_{\rm H_2O} < 5 \times 10^{13}$ cm^{-2}).
Conclusions. The overall analysis suggests that the emission in B2 comes from an extended (≥15″) region, whilst we cannot rule out the possibility that the emission in R arises from a smaller (>3″) region. In this context, H_2O seems to be important in tracing different gas components with respect to other molecules, e.g. such as SiO, a classical jet tracer. We compare a grid of C- and J-type shocks spanning different velocities (10 to 40 km s^{-1}) and two pre-shock densities (2×10^4 and 2×10^5 cm^{-3}), with the observed intensities. Although none of these models seem to be able to reproduce the absolute intensities of the water emissions observed, it appears that the occurrence of J-shocks, which can compress the gas to very high densities, cannot be ruled out in these environments.

Key words. ISM: molecules – stars: formation – ISM: jets and outflows – stars: low-mass – stars: individual: L1157

1. Introduction

Water controls the chemistry of many other species, whether in gas or solid phase, and it is recognised to be a unique diagnostic of warm gas and energetic processes occurring in regions of star formation (e.g., van Dishoeck et al. 2011). Water is a powerful probe of the physical variations and the temporal evolution of outflowing material, which is processed by shocks produced by fast protostellar jets impacting against high-density material. Water, unlike most molecules, cannot routinely be observed with ground-based facilities. However, space instruments, such as SWAS and Odin, have provided the first detection of the ground state line ortho-H_2O line at 557 GHz (e.g., Franklin et al. 2008; Bjerkeli et al. 2009). The profile of this ground state line has been compared to that of the CO line. This comparison is a direct testament to the H_2O abundance being enhanced by many orders of magnitude in the shock (Kristensen et al. 2010). The telescope ISO was also capable of detecting a number of water transitions excited in gas warmer than ∼80 K (e.g., Liseau et al. 1996), but with spectrally unresolved data.

The L1157 bipolar outflow is archetypical of the so-called chemically rich outflows (Bachiller & Pérez Gutiérrez 1997, hereafter BP97; Bachiller et al. 2001). At a distance of 250 pc, and being favorably oriented in the plane of the sky, the L1157 outflow is an ideal laboratory for observations of shocks chemistry. This outflow is known to be driven by a low-luminosity (∼4 $L_\odot$) Class 0 protostar and is associated with several blue-shifted (B0, B1, B2) and red-shifted (R0, R1, R, R2) lobes seen in CO (Gueth et al. 1998), and in IR H_2 images (e.g. Neufeld et al. 1994; Nisini et al. 2010).

The projected velocity of the northern (red-shifted) lobe is about 65% higher than that of the southern (blue-shifted) lobe (BP97) (see Fig. 1). However, the red-shifted lobe is more extended than the blue-shifted one and the kinematical ages of

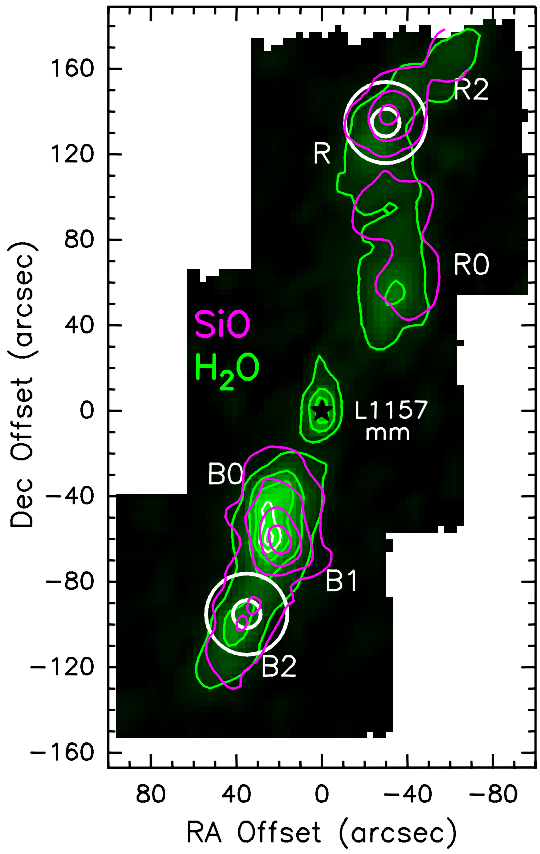

Fig. 1. PACS image of L1157 of the integrated H_2O emission at 1669 GHz (from Nisini et al. 2010). Offsets are with respect to the L1157-mm source, at coordinates $\alpha_{J2000} = 20^h39^m06\overset{s}{.}2$, $\delta_{J2000} = +68°02'16\overset{''}{.}0$. The contours of the SiO 3-2 integrated intensity is superimposed on the water map with a spatial resolution of 18″ (Bachiller et al. 2001). The positions chosen for the HIFI observations (R and B2) are marked by two white circles, which correspond to the largest and the smallest HIFI beam sizes.

the two lobes are found to be the same (15 000 yr) indicating that both lobes were created simultaneously. Each outflow lobe shows a clumpy structure and it seems that for each blue clump there is a corresponding red clump symmetrically located with respect to the central source. The symmetry in the individual clumps suggests that the outflow has undergone periods of enhanced ejection and the curved shape suggests that there have been variations in the direction of the driving wind. In addition, the morphology is clearly S-shaped that there is an underlying precessing jet. The brightest blue-shifted bow-shock, B1, was previously imaged at high-angular resolution revealing a clumpy arch-shape structure located at the top of an opened cavity (Tafalla & Bachiller 1995; Gueth et al. 1998; Benedettini et al. 2007; Codella et al. 2009). It has been found that L1157-B1 is well-traced by species released by dust mantles such as H_2CO, CH_3OH, and NH_3, complex molecules (Arce et al. 2008), and by SiO, which is the standard tracer of high-speed shocks (e.g., Gusdorf et al. 2008). In addition, L1157-B1 has been observed with HIFI and PACS spectrometers onboard the *Herschel* Space Observatory (Codella et al. 2010; Lefloch et al. 2010): the preliminary results confirm the rich chemistry associated with the B1 position, also showing bright H_2O emission.

The other bow-shocks have been less well-studied. As a consequence, it is still unclear how the physical and chemical properties vary along the axis of the L1157 outflow as well as between the blue- and red-shifted lobes.

We present the analysis of various water emission lines observed with HIFI towards two shocked regions in the L1157 outflow, which was observed as part of the the key program WISH (Water In Star-forming-regions with *Herschel*[1], van Dishoeck et al. 2011). The main aim of this paper is to constrain the physical parameters of the gas traced by water lines at the selected B2 and R positions of L1157. We investigate the different excitation conditions of H_2O in this shocked ambient gas in order to compare these conditions with other shock tracers. Since the abundance of water can be strongly affected by shocks, we are then able to infer the types of shocks that exist in the outflow regions traced by water emission.

2. Observations

Figure 1 presents the PACS map of the water emission at 1669 GHz (from Nisini et al. 2010). The H_2O map (green contour) is overlaid with contours of the emission from SiO (3–2) (magenta contour) (Bachiller et al. 2001) transitions. The water map exhibits several emission peaks corresponding to the positions of previously-known shocked knots, labelled B0-B1-B2 for the south-east blue-shifted lobe, and R0-R-R2 for the north-west red-shifted lobe. For our water line observations, we selected the shock positions B2 and R because they have different physical and chemical characteristics as shown in many previous works (e.g. Bachiller et al. 2001). Observations, from 500 to 1700 GHz, were carried out between May and November 2010 with the use of the HIFI instrument (de Graauw et al. 2010) in dual-beam switch mode with a nod of 3′ using fast chopping. The HIFI receivers are double sideband with a sideband ratio close to unity. The data were processed with the ESA-supported package HIPE[2] 5.1 (*Herschel* Interactive Processing Environment, Ott et al. 2010) for baseline subtraction and then exported after level 2 as FITS files in the CLASS90/GILDAS[3] format. Two polarizations, H and V, were measured simultaneously and then averaged together to improve the signal-to-noise ratio (S/N). We checked individual exposures for bad spectra, summed exposures, fitted a low-order polynomial baseline, and integrated line intensities as appropriate. The main beam efficiency (η_{mb}) depends on frequency and is calculated as described in Roelfsema et al. (2011), ranging from to 0.75 to 0.71 in the 535–1670 GHz range. The absolute calibration uncertainty was estimated to be ∼10%. At a velocity resolution of 1 km s^{-1}, the rms noise is 2–20 mK (T_A scale) for frequencies less than 1113 GHz and 60 mK at 1669 GHz.

3. Results

A total of 17 emission lines were detected. Table 1 lists the observed H_2O lines, associated with a wide range of excitation energies (27 K ≤ E_u ≤ 215 K). In addition, a detection of o–$H_2{}^{18}O$ 1_{10}–1_{01} in B2 helped us to constrain the optical depth. In the observed spectral bands, additional molecular transitions have been detected in the B2 bow-shock, such as NH_3 (1_0–0_0), HCO^+(6–5), CH_3OH–E ($11_{1,10}$–$10_{1,9}$), and $C^{18}O$ (5–4). On the other hand, the ^{13}CO (10–9) line was observed but not detected (see Table 2).

[1] http://www.strw.leidenuniv.nl/WISH/.

[2] HIPE is a joint development by the *Herschel* Science Ground Segment Consortium, consisting of ESA, the NASA *Herschel* Science Center, and the HIFI, PACS and SPIRE consortia.

[3] http://www.iram.fr/IRAMFR/GILDAS

Table 1. List of molecular species and transitions observed with HIFI in L1157 B2 and R.

Transition	ν_0[a] (MHz)	E_u[a,b] (K)	*HPBW* (″)	T_{peak} (mK)	rms[c] (mK)	V_{peak} (km s^{-1})	V_{max} (km s^{-1})	V_{min} (km s^{-1})	*FWHM* (km s^{-1})	F_{int} (mK km s^{-1})
B2 (α_{J2000} = 20^{h}39^{m}12^s.50, δ_{J2000} = +68° 00′ 41″.0)										
o–$H_2^{18}O$ (1_{10}–1_{01})	547 676.44	27	38	10.3(2)[d]	3	+1.8(0.3)[d]	+7	–4	5.4(0.6)[d]	59(7)[d]
o–H_2O (1_{10}–1_{01})	556 936.01	27	38	200(13)[e]	13	+2.7(1)[e]	+12	–9	–	8360(40)
p–H_2O (2_{11}–2_{02})	752 033.23	137	28	270(14)[d]	16	+2.4(0.2)[d]	+7	–7	4.8(0.2)[d]	1368(55)[d]
o–H_2O (3_{12}–3_{03})	1 097 364.79	215	19	125(17)[d]	19	+1.6(0.2)[d]	+13	–3	4.4(0.4)[d]	583(61)[d]
p–H_2O (1_{11}–0_{00})	1 113 342.96	53	19	75(20)[e]	20	+2.6(1.0)[e]	+12	–9	–	4510(33)
o–H_2O (2_{12}–1_{01})	1 669 904.77	80	13	47(60)[e]	60	+2.6(1.0)[e]	+11	–11	–	4221(120)
R(α_{J2000} = 20^{h}39^{m}01^s.00, δ_{J2000} = +68°04′31″.0)										
o–H_2O (1_{10}–1_{01})	556 936.01	27	38	256(5)	5	+19.6(1.0)	+35	–3	–	5027(31)
p–H_2O (2_{11}–2_{02})	7 52 033.23	137	28	176(13)	13	+7.7(1.0)	+30	+7	–	2103(60)
o–H_2O (3_{12}–3_{03})	1 097 364.79	215	19	154(22)[e]	22	+6.4(1.0)[e]	+21	–2	–	1633(99)
p–H_2O (1_{11}–0_{00})	1 113 342.96	53	19	228(15)	15	+19.6(1.0)	+27	–5	–	2555(74)
o–H_2O (2_{12}–1_{01})	1 669 904.77	80	13	–	<222	–	–	–	–	–

Notes. Peak velocity, intensity (in T_A scale), integrated intensity (not corrected for beam efficiency, F_{int}), minimum and maximum velocities (V_{min}, V_{max}), and linewidth (*FWHM*) are reported. [(a)] Frequencies and spectroscopic parameters have been extracted from the Jet Propulsion Laboratory molecular database (Pickett et al. 1998). [(b)] With respect to the ground H_2O level 1_{01} for the ortho-H_2O level and 0_{00} for the para-H_2O level, respectively. [(c)] At a spectral resolution of 1 km s^{-1} . [(d)] Gaussian fit when the observed profile is Gaussian-like. [(e)] Measurements taken at the dip of the emission line.

Table 2. List of molecular species and transitions observed with HIFI in L1157 B2 and R.

Transition	ν_0[a] (MHz)	E_u[a] (K)	*HPBW* (″)	T_{peak} (mK)	rms[b] (mK)	V_{peak} (km s^{-1})	V_{max} (km s^{-1})	V_{min} (km s^{-1})	*FWHM* (km s^{-1})	F_{int} (mK km s^{-1})
Bow-shock B2										
HCO^+ (6–5)	535 061.40	90	37	19(2)[c]	3	+2.2(0.1)[c]	+7	–2	3.3(0.3)[c]	67(6)[c]
CH_3OH-E ($11_{1,10}$ – $-10_{1,9}$)	536 191.07	169	37	10(2)[c]	3	+1.6(0.3)[c]	+7	–4	4.3(0.7)[c]	48(6)[c]
$C^{18}O$ (5–4)	548 830.97	79	37	24.3(2)[c]	3	+2.4(0.1)[c]	+5	–0	2.5(0.3)[c]	66(3)[c]
NH_3 (1_0–0_0)	572 498.07	28	38	83.6(8)[c]	8	+0.9(0.2)[c]	+7	–6	6.2(0.4)[c]	549(31)[c]
^{13}CO (10–9)	1 101 349.65	291	21	–	20	–	–	–	–	–
Bow-shock R										
NH_3 (1_0–0_0)	572 498.07	28	38	28(8)	8	+6.6(1.0)	+9	–0	–	105(9)

Notes. Peak velocity, intensity (in T_A scale), integrated intensity (not corrected for beam efficiency, F_{int}), minimum and maximum velocities (V_{min}, V_{max}), and linewidth (*FWHM*) are reported.[(a)] Frequencies and spectroscopic parameters have been extracted from the Jet Propulsion Laboratory molecular database (Pickett et al. 1998). [(b)] At a spectral resolution of 1 km s^{-1}. [(c)] Gaussian fit when the observed profile is a Gaussian-like.

3.1. Water profiles

The B2 and R water spectra shown in Fig. 2 (here in units of antenna temperature, T_A) were smoothed to a velocity resolution of 1 km s^{-1}, to allow comparisons among all water transitions.

The spectra measured in R are consistently fainter than those measured in B2 and the water transition at 1669 GHz appears to be barely detected at R. In the B2 spectra, the profiles show a weak red emission and those lines with $E_u \leq 80$ K show absorption at ambient velocity. The B2 spectra also show bright emission and peaks close to the systemic velocity, while the bulk of the R emission is definitely red-shifted. The B2 spectra have a narrower velocity range than those observed at the R position. This could reflect a different shock velocity or simply be a consequence of a different inclination on the plane of sky.

Interestingly, the 557 GHz profile observed at B2 is associated with a much narrower wing (highest blue-shifted velocity, −9 km s^{-1}) than that observed in B1 (−25 km s^{-1}), studied in the framework of the CHESS GT Key Project (see Fig. 3; Codella et al. 2010; Lefloch et al. 2010). This could be an indication of lower shock velocities at B2. On the other hand, B2 has a broader red wing than B1, supporting the idea that the profiles are strongly affected by geometrical effects. Further comparison of H_2O profiles from observations obtained in B1 and B2, would be instructive and will be performed when the full set of CHESS water data become available.

We note that the profiles in B2 become increasingly narrow with increasing line excitation, while the line widths (FWZI) in R remain almost constant. In particular, the emission produced by transitions to the ground state level are those that appear broader (see Fig. 2). These spectra are also those affected by the absorption dip that have a higher S/N level. However, we cannot say wheter the narrow feature is a real feature.

It is also notable that the spectra in R have multiple peaks that present a clear dichotomy with one peak at ∼+20 km s^{-1} associated with transitions with $E_u \leq 60$ K and a lower velocity peak at ∼+10 km s^{-1} associated with transitions with $E_u \geq 136$ K. Surprisingly the high velocity emission, usually assumed to be emitted from regions close to the fast jet driving the shocks, is associated with the low excitation emission lines. The dichotomy observed in the R bow shock has not been detected in any of the molecules observed so far in L1157. However, as already observed in B2, the difference in the line profiles at various excitation energies could be caused by a large amount of self-absorption for the low velocity range of those lines, which are related to the ground state level. We actually observe a dip in the water emission line at 557 GHz at the systemic velocity. To explain the striking difference (over 10−20 km s^{-1}) between the line shapes as observed in R, we would have to assume that the absorption were caused by outflowing gas. It is evident that an additional multiline analysis would be required to test this assumption. We also note that the same dichotomy was observed in L1148 at the R4 position by Santangelo et al. (2012), where they clearly show that this trend is real.

Figure 4 shows the intensity ratio measured towards B2 and R of transitions selected to have different excitation but observed within similar half power beam width (HPBW), to minimise the effects of beam dilution. The ratios are plotted only for velocities

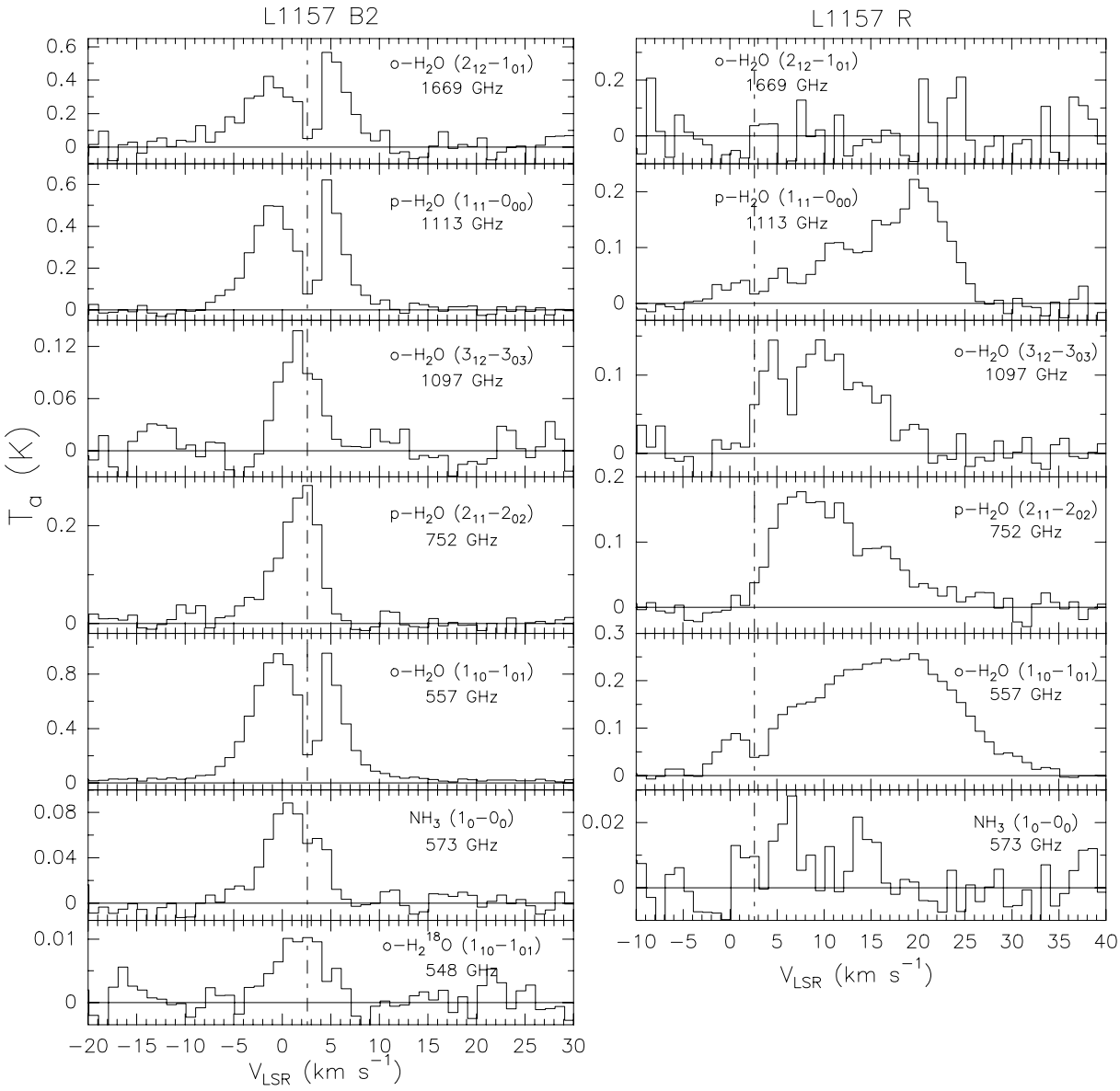

Fig. 2. Molecular line profiles observed towards L1157-B2 and R: species and transitions are reported in the panels. The vertical dashed line indicates the ambient LSR velocity (+2.6 km s^{-1} from C^{18}O emission; BP97).

at which both lines have $S/N > 3$. We note that, besides the obvious effects due to the presence of the absorption dip, the o–H_2O (2_{12}–1_{01})/p–H_2O (1_{11}–0_{00}) water ratio seems to increase with velocity, while in R it is clear that the p–H_2O (2_{11}–2_{02})/p–H_2O (1_{11}–0_{00}) water ratio decreases in both the low and high velocity components with respect to the peak at ∼8 km s^{-1}. This effect, which has an estimated line ratio error ≤30%, reflects the distinctive dichotomy that was observed in the R bow-shock where water transitions with different energy excitations peak at two different velocities.

In B2, the o–H_2O (1_{10}–1_{01})/o–$H_2{}^{18}O$ (1_{10}–1_{01}) ratio is used to estimate the H_2O optical depth, τ_{16}, assuming that the two water isotopologues are tracing the same material with the same excitation temperature. To derive the o–$H_2{}^{16}O$ opacity, we need to use the $^{16}O/^{18}O$ ratio for which we take the assumed local ISM value of 560 (Wilson & Rood 1994). The measured τ_{16} value in the low velocity line wings is about 2, which is in agreement with our non-LTE excitation analysis. However, as it cannot be confirmed that the o–$H_2{}^{16}O$ line and the o–$H_2{}^{18}O$ line are associated with the same excitation temperatures, any constraints placed on this value of opacity to infer the column density at B2 would be highly uncertain.

3.2. Other line profiles

Finally, the spectral set-up allowed us to observe the NH_3 (1_0–0_0) fundamental line: a tentative detection (3σ) of NH_3 is found at R, while relatively bright emission is detected at B2 as found in the nearby blue shock B1 (see Fig. 3, Codella et al. 2010). The ammonia emission, in the L1157 outflow, will be analysed in a forthcoming paper. Table 2 lists the serendipitous detections observed at the B2 bow-shock HCO^+ (6–5), CH_3OH-E ($11_{1,10}$–$10_{1,9}$), ^{13}CO (10–9), and $C^{18}O$ (5–4), that was used to infer the water abundances. The B2 additional spectra are shown in Fig. 5 (here in terms of antenna temperature, T_a). Spectra were smoothed to a velocity resolution of 1 km s^{-1}; they all peak at the systemic velocity and are all associated with a relatively narrow line width (≤6 km s^{-1}) with respect to the water spectra.

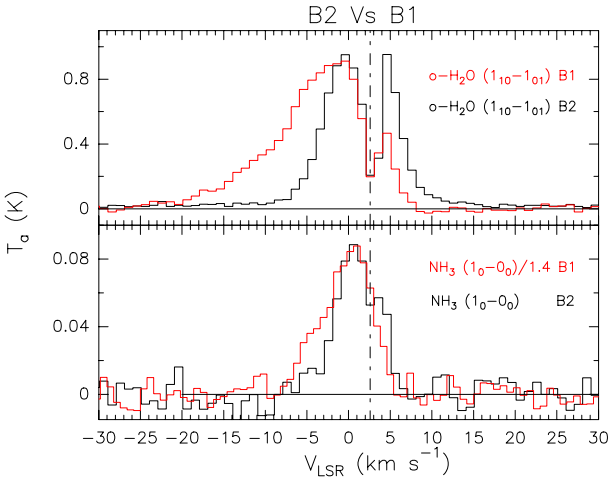

Fig. 3. Comparison of water emission lines at 557 GHz and NH_3 (1_0–0_0) observed at L1157-B1 (red profiles) and B2 (black profiles). The vertical dashed line indicates the ambient LSR velocity (+ 2.6 km s^{-1} from $C^{18}O$ emission; BP97).

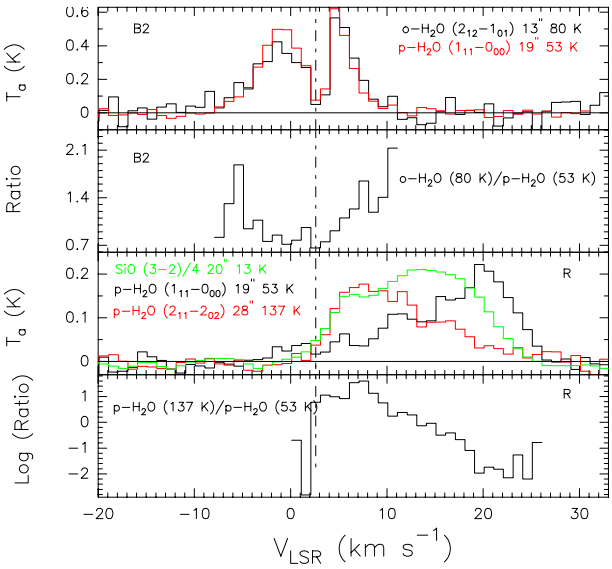

Fig. 4. Line temperature water ratios and water profiles in R and B2. Line temperature ratios, as function of velocity, are only shown where the S/N is larger than three for both types of emission.

4. Excitation analysis

We ran the RADEX non-LTE model (van der Tak et al. 2007) with collisional rate coefficients by Faure et al. (2007) using the escape probability method for a plane parallel geometry in order to constrain the physical parameters ($T_{\rm kin}$, $N_{\rm H_2O}$ and $n_{\rm H_2}$) of water emission. An ortho/para = 3 ratio was assumed, equal to the high temperature equilibrium value. To place some constraints on the unknown size of the emitting region, we assumed three different sizes (3″, 15″, and 30″). RADEX does not take into account the near-IR pumping of the H_2O lines where the radiation field is relatively strong and has some impact on the excitation conditions of the emitting gas. However, since both the B2 and R positions are relatively far from the central source, we expect no continuum to affect our results.

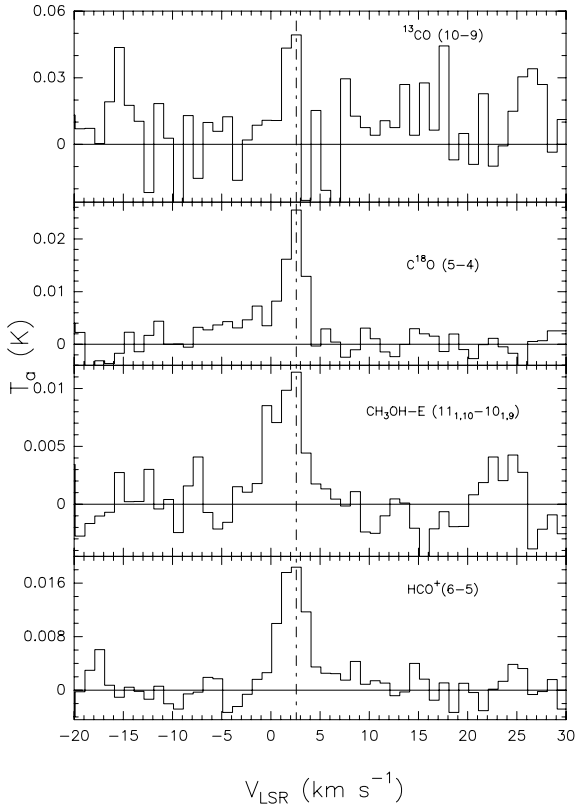

Fig. 5. Additional emission lines (beside the H_2O and NH_3 profiles reported in Fig. 2) observed at L1157-B2.

4.1. L1157 B2

At B2, given the presence of the absorption dip and the relatively narrow velocity range, we model the physical parameters of water emission by integrating the H_2O intensity over the whole spectral profile (i.e. neglecting the absorption dip). We consider the measurements of water transitions with an absorption dip as upper limits. In Fig. 6, we overplot non-LTE RADEX model predictions against integrated flux water ratios. For this analysis, we conservatively assumed an uncertainty of 20%. Coloured triangles with uncertainties are the observed values corrected for beam filling and assuming three different sizes as mentioned in the insert of the plots. The top panel of Fig. 6 shows a plot of the o–H_2O (3_{12}–3_{03})/p–H_2O (1_{11}–0_{00}) ratio versus o–H_2O (3_{12}–3_{03}), the middle panel shows a plot of the o–H_2O (2_{12}–1_{01})/o–H_2O (1_{10}–1_{01}) ratio versus o–H_2O (2_{12}–1_{01}), and the bottom panel shows a plot of the o–H_2O (3_{12}–3_{03})/o–H_2O (2_{12}–1_{01}) versus o–H_2O (3_{12}–3_{03})/o–H_2O (1_{10}–1_{01}) ratios.

Some general conclusions can be drawn from the inspection of Fig. 6. The observations are consistent with model predictions only when we assume an emission size >3″ (black triangle). In particular, there appears to be a size closer to 15″–30″ in agreement with the L1157 map of the o–H_2O (2_{12}–1_{01}) line published by Nisini et al. (2010) (see bottom panel). The observed water ratio appears to be well constrained by the low values of column density $N_{\rm H_2O} \leq 5 \times 10^{13}$ cm^{-2} (see the top panel), while a density range of $10^5 \leq n_{\rm H_2} \leq 10^7$ cm^{-3} and temperatures $T_{\rm kin} \geq 300$ K are inferred from all panels. However, owing to the absorption dip in both water transitions plotted in the middle panel, the inferred physical conditions can only be considered as upper limits. The absorption dip might affect our analysis, by shifting observations towards lower excitation conditions.

Table 3. Physical conditions traced by water lines.

B2	R-LV	R-HV
$T_{\rm kin} \geq 300$ K	$T_{\rm kin} \geq 300$ K	$T_{\rm kin} \geq 100$ K
$10^5 \leq n_{\rm H_2} \leq 10^7$ cm^{-3}	$n_{\rm H_2} \sim 10^8$ cm^{-3}	$N_{\rm H_2O} \sim 5\times10^{13}$ cm^{-2}, $n_{\rm H_2} \sim 10^6$ cm^{-3}
$N_{\rm H_2O} \leq 5\times10^{13}$ cm^{-2}	$N_{\rm H_2O} < 5\times10^{13}$ cm^{-2}	$N_{\rm H_2O} \sim 5\times10^{12}$ cm^{-2}, $n_{\rm H_2} \sim 10^7$ cm^{-3}
Inferred size 15″–30″	Inferred size >3″	Inferred size ≥15″

By assuming that the absorption dip observed in the water ground state transition is due to foreground gas unrelated to L1157-B2, we estimate, from the standard radiative transfer equation, that the temperature is 8 K $\leq T_{\rm ex} \leq$ 13 K when adopting a $0.1 \leq \tau_{16} \leq 10$. This low value of $T_{\rm ex}$ usually implies low densities or low kinetic temperatures. No other constraints can be inferred owing to the uncertainties in the measurements and the large number of free parameters that have to be fitted simultaneously with the RADEX code.

4.2. L1157 R

In the water profiles of the bow-shock R, Fig. 2 shows an evident dichotomy at different excitations where two emission peaks at different velocities clearly displaying different excitation conditions. Thus, we modelled the emission by splitting the lines into two components (hereafter called LV, at ∼+10 km s^{-1}, and HV, at ∼+20 km s^{-1}). In Fig. 7, we overplotted the non-LTE RADEX model predictions on the observed LV and HV $T_{\rm mb}$ water ratios. The top panel of Fig. 7 shows a plot of the o−H_2O (3_{12}−3_{03})/o−H_2O (1_{10}−1_{01}) ratio versus o−H_2O (3_{12}−3_{03}), while the bottom panel of Fig. 7 shows a plot of the p−H_2O (1_{11}−0_{00})/o−H_2O (3_{12}−3_{03}) ratio versus p−H_2O (1_{11}−0_{00}).

A first conclusion that can be drawn is that the LV component appears to be associated with higher excitation conditions than the HV component and we can exclude a point-like source (i.e. the 3″ case) based on the inconsistency of the column density, which can be derived from the two panels. For the low excitation HV, we have standard kinetic temperatures ≥100 K and a degeneracy between column density and hydrogen density: either $N_{\rm H_2O} \sim 5\times10^{13}$ cm^{-2} and $n_{\rm H_2} \sim 10^6$ cm^{-3} or $N_{\rm H_2O} \sim 5\times10^{12}$ cm^{-2} and $n_{\rm H_2} \sim 10^7$ cm^{-3}. On the other hand, for the high excitation LV emission the observed water ratio traces temperatures $T_{\rm kin} \geq 300$ K, as well as surprisingly dense gas with $n_{\rm H_2} \sim 10^8$ cm^{-3} and low column density, $N_{\rm H_2O} < 5\times10^{13}$ cm^{-2}. The tentative detection of NH_3 (1_0−0_0) emission at these velocities seems to support a very high density solution.

5. On the origin of water emission in L1157

In summary, Table 3 outlines the physical conditions traced by water that we constrain from our analysis. The water at B2 traces lower density environments than both R-LV and R-HV. In addition, the main difference between R-LV and R-HV is that H_2O at R-HV traces lower temperatures and densities than R-LV. The physical parameters derived in B2 and R-HV are in reasonable agreement with those measured by Nisini et al. (2007), using multi-transition observations of a classical jet tracer such as SiO. However, the density inferred for R-LV ($n_{\rm H_2} \sim 10^8$ cm^{-3}) is higher than that derived from SiO emission by two orders of magnitude. In reality, the SiO profiles observed at the R position (see Fig. 4) cast in serious doubt that emission from these species has a common physical origin. In addition, our results strongly support the conclusion of Nisini et al. (2010) that water emission seems to follow quite closely the distribution of H_2 emission.

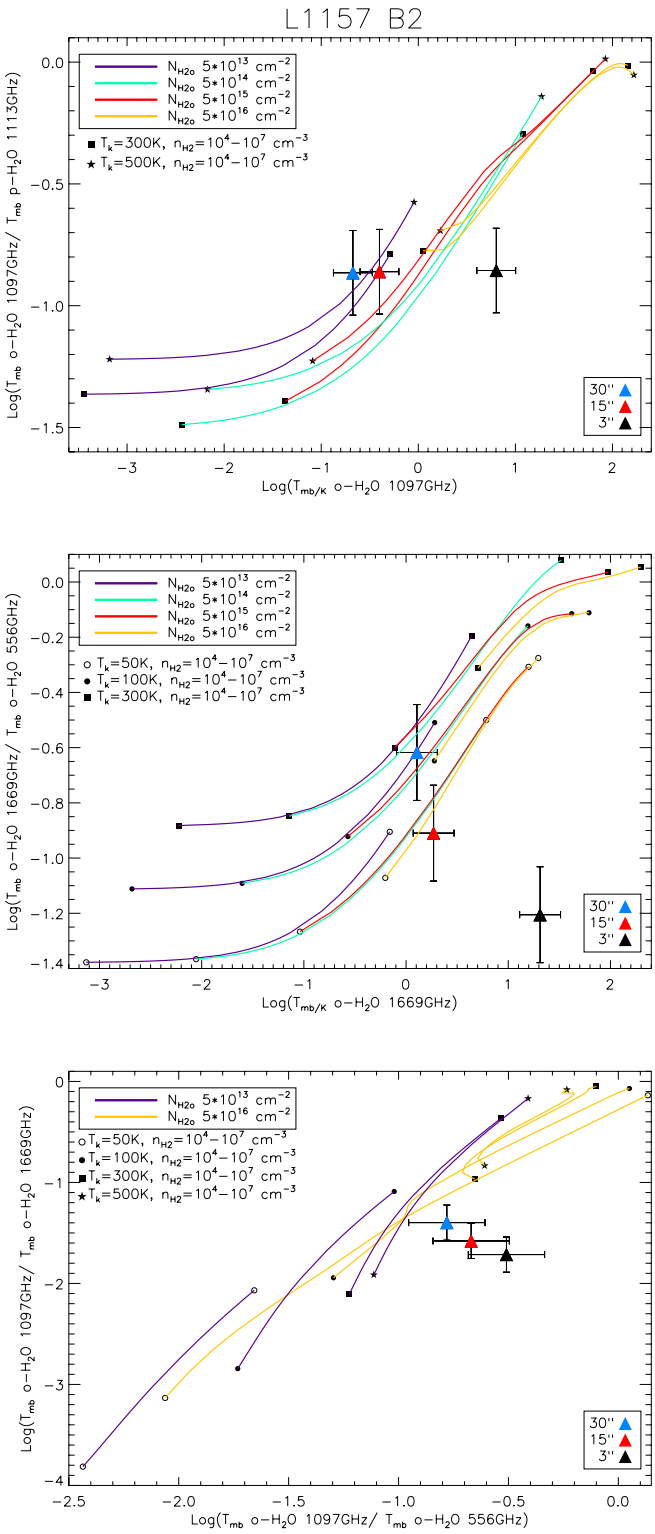

Fig. 6. Analysis of the water line emissions in L1157 B2. o−H_2O (3_{12}−3_{03})/p−H_2O (1_{11}−0_{00}) ratio versus o−H_2O (3_{12}−3_{03}) (in logarithmic scale, top panel), o−H_2O (2_{12}−1_{01})/o−H_2O (1_{10}−1_{01}) ratio versus o−H_2O (2_{12}−1_{01}) (*middle panel*), and o−H_2O (3_{12}−3_{03})/o−H_2O (1_{10}−1_{01}) versus o−H_2O (3_{12}−3_{03})/o−H_2O (2_{12}−1_{01}) ratios (*bottom panel*), for non-LTE (RADEX) plane-parallel models at the labelled temperatures. A linewidth of 5.5 km s^{-1} has been assumed, according to the observed spectra. Each coloured curve corresponds to the labelled $N_{\rm H_2O}$ (see insert at the top-left corner). H_2 density increases from left to right as the labelled values. Triangles with error bars indicate the size of the emitting region (30″, 15″, 3″).

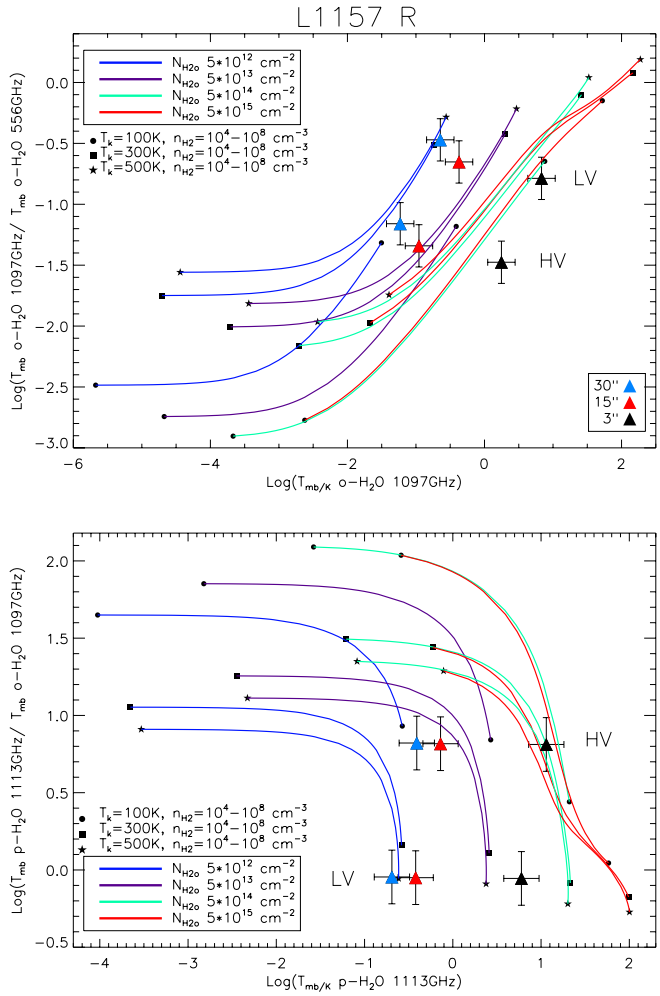

Fig. 7. Analysis of the water line emission in L1157 R. o–H_2O (3_{12}–3_{03})/o–H_2O (1_{10}–1_{01}) ratio versus o–H_2O (3_{12}–3_{03}) (in logarithmic scale, *top panel*), and p–H_2O (1_{11}–0_{00})/o–H_2O (3_{12}–3_{03}) ratio versus p–H_2O (1_{11}–0_{00}) (*bottom panel*), for non-LTE (RADEX) plane parallel models at the labelled temperatures. A linewidth of 10 km s^{-1} has been assumed, consistent with the observed spectra. Each coloured curve corresponds to the labelled N_{H_2O} (see insert). H_2 density increases from left to right as the labelled values. Triangles with error bars indicate the size of the emitting region (30″, 15″, 3″).

The general physical conditions inferred in the R bow shock ($T_{kin} \geq 300$ K, $n_{H_2} \sim 10^6$–10^7 cm^{-3}) are consistent with those derived for the H_2 in Nisini et al. (2010).

5.1. Water abundances

We derive, at the R bow shock position, the H_2O abundance, with respect to H_2, using the $N(H_2)$ estimated by Nisini et al. (2007) and in B2 using the $C^{18}O$ (5-4) line emission detected in the present survey (see Fig. 5 and Tab. 2). The velocity averaged H_2O abundance for R is $\sim 10^{-6}$–10^{-7}.

The H_2O abundance for B2 is estimated to be $\sim 10^{-6}$ assuming $[C^{18}O]/[H_2] = 2 \times 10^{-7}$ (Wilson & Rood 1994) in the temperature range from 300 to 500 K (see Table 3). This result is consistent with the water abundance found at B1 at low velocities (Lefloch et al. 2010). On the other hand, the X(H_2O) measured at the highest velocities in B1 is two orders of magnitude greater than in B2 ($\sim 10^{-4}$). These differences could provide evidence for an older shock in B2 than the one in B1.

The results found in R are comparable with those obtained by Santangelo et al. (2012) in the L1448 outflow. These low water abundances could support the possibility that there is a J-shock instead of a C-shock where the H_2O abundance is expected to be $\sim 10^{-4}$ relative to H_2. Alternatively, the low measured water abundances could also be evidence of either an old shock where the water in the gas phase has had time to be depleted on grains or of UV dissociation of H_2O (see Bergin et al. 1998).

5.2. Comparison with shocks models

Theoretical studies have indicated that, under typical interstellar conditions, shocks faster than ~20 km s^{-1} are efficient enough to free much of the water ice frozen onto grain surfaces (Draine et al. 1983), while shocks faster than ~15 km s^{-1}, through gas-phase chemical reactions, produce large quantities of water (Kaufman & Neufeld 1996). After the shocked gas has cooled, enhanced water abundances of $\sim 10^{-4}$ relative to H_2 can persist for as long as 10^5 yr (Bergin et al. 1998). Sub-millimeter and far-infrared water emission lines are very efficient coolers, hence high interstellar water abundances produced by the shock processing are relevant to the thermal evolution of the gas (e.g., Neufeld et al. 1995). Observations of a number of excited molecular transitions in L1157 clearly indicate that shocks are present in both lobes. The present dataset should be compared in a more detailed way with shock models. In this present paper, we only discuss our data using models provided in the literature.

We have compared a grid of C- and J-type shocks spanning different velocities (10 to 40 km s^{-1}) and two pre-shock densities (2×10^4 and 2×10^5 cm^{-3}) provided by Flower & Pineau des Forêts (2010), with the observed intensities. Figure 8 shows the observed line ratios with respect to the high energy (E_u = 215 K) 1097 GHz line for different sizes of B2, R-LV and R-HV against the predicted shock line ratios. From our analysis, none of these models seem to be able to properly reproduce the absolute intensities of the water emissions observed.

In the case of the R-HV component, a degeneracy is particularly noticeable because, for an emitting region of size 30″, both a speed of 10 km s^{-1} with a pre-shock density of 2×10^5 cm^{-3} and a speed of 30 km s^{-1} with a pre-shock density of 2×10^4 cm^{-3} can be inferred for both types of shock. This is consistent with the analysis made in the water diagnostic plots (Fig. 7). The same sort of degeneracy can be drawn for the R-LV component, where we do not find a satisfactory solution that matches the full sample of water transitions. The most plausible explanation is given by, in agreement with Fig. 7, a size of 3″ for a C-type shock with a speed of 30 km s^{-1} and pre-shock density of 2×10^4 cm^{-3}, and for a J-type shock with a speed of 20 km s^{-1} and pre-shock density of 2×10^5 cm^{-3}.

Regarding the B2 position, a lower speed of J-shocks around 10 km s^{-1} is inferred. Two different solutions are found: (i) a pre-shock density of 2×10^4 and 3″ of size, or (ii) a pre-shock density of 2×10^5 and 15″ of size. According to our previous water analysis, an emitting size of 15″ is more plausible. These preliminary results imply that more detailed modelling and a more complete analysis should be performed. Note, for instance, that UV H_2O dissociation is not taken into account in the grid of shock models used.

C-shocks were recently invoked by Flower & Pineau des Forêts (2010) and Viti et al. (2011) modelling L1157 B1. On the other hand, results obtained with PACS in the course of the CHESS spectral survey key-program (Benedettini et al. in prep.) required J-shocks to explain the CO excitation conditions in L1157 B1. This scenario could also provide a

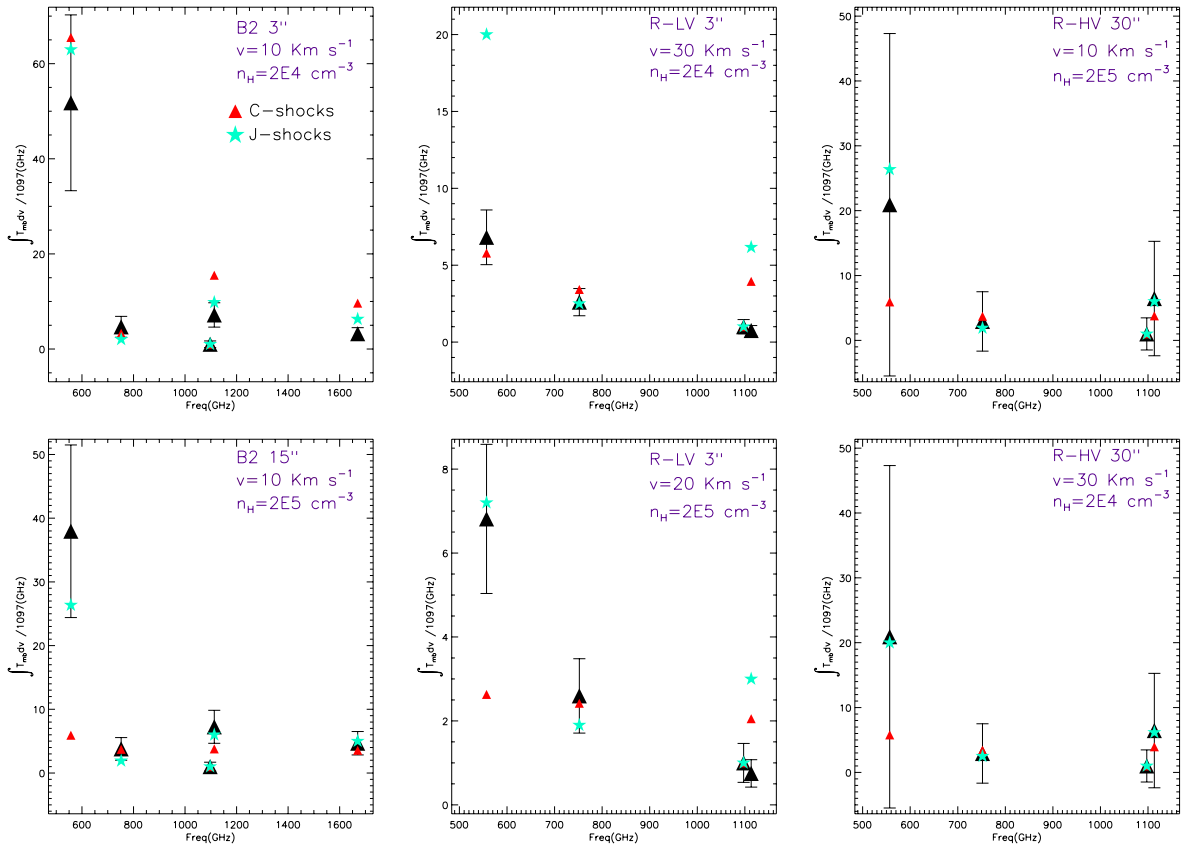

Fig. 8. Comparison between the observed HIFI H_2O line ratios of the two velocity components in R and B2 for different sizes (black triangles) and those predicted by C-type (red triangle) and J-type (cyan triangles) shock models from Flower & Pineau des Forêts (2010).

possible explanation of our analysis in B2 and R, where both C- and J -type shocks seem to be required.

6. Conclusions

We have presented observations of water emission in the 500–1700 GHz band towards the two bow-shocks B2 and R, of the L1157 proto-stellar outflow. The main conclusions are the following:

1. The comparison between H_2O and SiO profiles, and their physical characteristics casts serious doubt on the assumption that emission from these species has a similar physical origin.
2. We have derived H_2O abundances of $R \sim 10^{-6}$–10^{-7} and for B2 $\sim 10^{-6}$. This result is consistent with the water abundance found at B1 at low velocities. On the other hand, the X(H_2O) measured at the highest velocities in B1 is two orders of magnitude greater than in B2 ($\sim 10^{-4}$). These differences could provide evidence for an older shock in B2 compared to that in B1.
3. The emerging scenario highlights the importance of J-shocks, which are expected to be associated with a thin layer and very densely compressed material in these environments. The results found in R are comparable with those obtained by Santangelo et al. (2012) in the L1448 outflow. These low water abundances could support the possibility of having a J-shock instead of a C-shock.
4. Interestingly, the highest excitation conditions are observed at low velocities. However, if we were to assume that high excitation is tracing portions of gas near the shock, we could solve this apparent contradiction by assuming that we have observed a very collimated region located along the plane of the sky. In this case, the fast collimated gas should be reprojected and thus have lower radial velocities. On the other hand, a less excited region could be more extended, which would result in a wider velocity range due to the geometry.

Acknowledgements. The authors are grateful to Sylvie Cabrit and the WISH internal referees Laurent Pagani and Carolyn M^{c}Coey for their constructive comments on the manuscript. MV would like to thank Dr. S. Farrens for comments. WISH activities in Osservatorio Astrofisico di Arcetri are supported by the ASI project 01/005/11/0. B.N. and G.S. also acknowledge financial contribution from the agreement ASI-INAF I/009/10/0. HIFI has been designed and built by a consortium of institutes and university departments from across Europe, Canada and the United States under the leadership of SRON Netherlands Institute for Space Research, Groningen, The Netherlands and with major contributions from Germany, France and the US. Consortium members are: Canada: CSA, U.Waterloo; France: CESR, LAB, LERMA, IRAM; Germany: KOSMA, MPIfR, MPS; Ireland, NUI Maynooth; Italy: ASI, IFSI-INAF, Osservatorio Astrofisico di Arcetri-INAF; Netherlands: SRON, TUD; Poland: CAMK, CBK; Spain: Observatorio Astronomico Nacional (IGN), Centro de Astrobiologia (CSIC-INTA). Sweden: Chalmers University of Technology – MC2, RSS & GARD; Onsala Space Observatory; Swedish National Space Board, Stockholm University - Stockholm Observatory; Switzerland: ETH Zurich, FHNW; USA: Caltech, JPL, NHSC.

References

Arce, H. G, Santiago-García, J., Jørgensen, J. K., et al. 2008, ApJ, 681, L21
Bachiller, R., & Peréz Gutiérrez, M. 1997, ApJ, 487, L93 (BP97)
Bachiller, R., Peréz Gutiérrez, M., Kumar, M. S. N., et al. 2001, A&A, 372, 899
Benedettini, M., Viti, S., Codella, C., et al. 2007, MNRAS, 381, 1127

Bergin, E. A., Neufeld, D. A., & Melnick, G. J. 1998, ApJ, 499, 777
Bjerkeli, P., Liseau, R., Olberg, M., et al. 2009, A&A, 507, 1455
Codella, C., Benedettini, M., Beltrán, M. T., et al. 2009, A&A, 507, L25
Codella, C., Lefloch, B., Ceccarelli, C., et al. 2010, A&A, 518, L112
de Graauw, Th., Helmich, F. P., Phillips, T. G., et al. 2010, A&A, 518, L6
Draine, B. T., Roberge, W. G., & Dalgarno, A. 1983, ApJ, 264, 485
Faure, A., Crimier, N., Ceccarelli, C., et al. 2007, A&A, 472, 1029
Flower, D. R., & Pineau des Forêts, G. 2010, MNRAS, 406, 1745
Franklin, J., Snell, R. L., Kaufman, M. J., et al. 2008, ApJ, 674, 1015
Gueth F., Guilloteau S., & Bachiller R. 1998, A&A, 333, 287
Gusdorf, A., Cabrit, S., Flower, D., et al. 2008, A&A, 482, 809
Kaufman, M. J., & Neufeld, D. A. 1996, ApJ, 456, 611
Kristensen, L. E., Visser, R., van Dishoeck, E. F. et al. 2010, A&A, 521, L30
Lefloch, B., Cabrit, S., Codella, C., et al. 2010, A&A, 518, L113
Liseau, R., Ceccarelli, C., larsson, B., et al. 1996, A&A, 315, 181
Neufeld, D. A., & Green, S. 1994, ApJ, 432, 158
Neufeld, D. A., Lepp, S., & Melnick, G. J. 1995, ApJS, 100, 132
Nisini, B., Codella, C., Giannini, T., et al. 2007, A&A, 462, 163
Nisini, B., Benedettini, M., Codella, C., et al. 2010a, A&A, 518, L12
Nisini, B., Giannini, T., Neufeld, D. A., et al. 2010b, ApJ, 724, 69
Ott, S. 2010, in Astronomical Data Analysis Software and Systems XIX, ed. Y. Mizumoto, K.-I. Morita, & M. Ohishi, ASP Conf. Ser., 434, 139
Pickett, H. M., Poynter, R. L., Cohen, E. A., et al. 1998, JQSRT, 60, 883
Roelfsema, P. R., Helmich, F. P., Teyssier, D., et al. 2011, A&A, 537, A17
Santangelo, G., Nisini, B., Giannini, T., et al. 2012, A&A, in press, DOI: 10.1051/0004-6361/201118113
Tafalla, M., & Bachiller, R. 1995, ApJ, 443, L37
Zhang, Q., Ho, P. T. P., & Wright, M. C. H. 2000, ApJ, 119, 1345
van Dishoeck, E. F., Kristensen, L. E., Benz, A. O., et al. 2011, PASP, 123, 138
van der Tak F. F. S., Black, J. H., Schøier F. L., et al. 2007, A&A, 468, 627
Viti, S., Jimenez-Serra, I., Yates, J. A., et al. 2011, ApJ, 740, L3
Wilson, T. L., & Rood, R. T. 1994, ARA&A, 32, 191